THE JOURNAL OF PHYSICAL CHEMISTRY C
A JOURNAL OF THE AMERICAN CHEMICAL SOCIETY

pubs.acs.org/JPCC

Article

Predicted Superconductivity in the Electride Li_5C

Zenner S. Pereira, Giovani M. Faccin, and Edison Z. da Silva*

Cite This: *J. Phys. Chem. C* 2021, 125, 8899–8906

Read Online

ACCESS | Metrics & More | Article Recommendations | Supporting Information

ABSTRACT: Superconductivity under pressure is a very important research path for finding new superconductors, and electrides have been shown to present superconductivity under pressure. In the present work, using density functional theory (DFT) in association with the particle swarm search method (PSO), we discovered a remarkable electride superconductor Li_5C with *P6/mmm* symmetry. This newly predicted material has stability in the range from 50 to 210 GPa, confirmed by phonon analysis and ab initio molecular dynamics. This electride has a two-dimensional (2D) hexagonal anionic electron topology, creating connected electronic channels in the interstitial sites of the crystal. We also show that Li_5C has a significant conventional electron−phonon coupling with superconducting critical temperatures (T_c) estimated up to 48.3 K at 210 GPa, which is the highest T_c value already reported for lithium−carbon compounds and one of the highest known transition temperatures predicted for electrides. Even at moderate pressure (50 GPa), this material shows a relatively high T_c value (14.2 K).

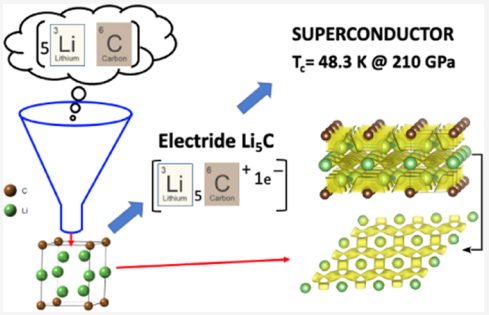

INTRODUCTION

Electrides are a special case of ionic compounds in which one or more electrons can be quantum-confined in the interstitial sites of a crystal.[1,2] In general, electrides have a huge difference in electronegativity or electropositivity in their composition atoms. Although they are very similar to classical ionic compounds, electrides have a striking feature: in these compounds, some electrons are not completely transferred from cations to anions and also do not make covalent bonds. Also, these electrons can reside in the interstitial sites of the crystal as in quantum confinement problems. In a conventional concept of electrides, the interstitial electrons behave like anions.[3]

It has already been demonstrated that electrides can have diverse dimensional anionic density topologies; therefore, an electride can be labeled in accordance with the following characteristics: 0D (cavities), 1D-linked (one-dimensional), two-dimensional (2D), or three-dimensional (3D) configuration.[4,5] As a consequence of interstitial ionic electrons not being bound to atomic cores, they are relatively free in the interstitial region, leading to electride materials that have low work functions and high conductivity. These characteristics enable electrides to be used in various applications such as electron emitters,[6] anode materials in batteries,[7,8] superconductors,[9−13] decomposition of CO_2 (splitting CO_2),[14] and organic light-emitting diodes (OLEDs).[15] Some 2D electrides have demonstrated high conductivity and potential to work as anode materials for batteries.[7,8] As a suitable example, we can cite Ca_2N,[16,17] which is an electride with interconnected 2D electron gas layers and presents excellent electron conductivity.

Superconductivity was explained as due to the electron−phonon (EP)-mediated attractive electron−electron interaction by Bardeen Cooper and Schrieffer (BCS) in 1957.[18] Its extensions were implemented by Gorkov's green function formalism[19] and Eliashberg theory.[20] Empirical models for T_c were proposed. The McMillan equation[21] and later the Allen and Dynes equation[22] are schemes that, incorporated in today's density functional theory (DFT) formalism, are excellent tools to search for superconductivity in new materials. With parameters from DFT, this formalism is presently used to estimate transition temperatures of more complex materials such as electrides under pressure.

High conductivity or superconductivity are important characteristics to be achieved in electrides. It has already been demonstrated that even 0D electrides can display superconductor behavior. For instance, Miyakawa showed that $[Ca_{24}Al_{28}O_{64}]^{4+}(e^-)_4$ is a 0D electride with a critical temperature of superconductivity up to 0.4 K.[23] Recently, Li_6P in the *C2/c* phase was predicted to be an electride superconductor with T_c = 39.3 K at 270 GPa, a work in which the authors claimed to have achieved the highest T_c for electrides.[13] However, a predicted metastable phase for Li_3S achieves T_c = 80 K at 500 GPa, as pointed out years ago by Kokail and co-workers.[12] Very recently, as pointed out by

Received: March 15, 2021
Revised: April 1, 2021
Published: April 20, 2021

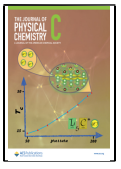

https://doi.org/10.1021/acs.jpcc.1c02329
J. Phys. Chem. C 2021, 125, 8899–8906

Zhang[5] and also to our knowledge, at high pressures, only few electrides have been reported to be superconductors and most of them have low T_c values.[9−13,24,25]

In this sense, we present a new predicted 2D electride, Li_5C, which at high pressures is a superconductor with hexagonal symmetry ($P6/mmm$). This compound shows stability in the range from 50 to 210 GPa under phonon analysis and ab initio molecular dynamics (AIMD) simulations. Li_5C also displays 2D hexagonal anionic density located in the crystal interstitial sites. In this material, pressure is a potential macroscopic parameter to control T_c. The maximum T_c achieved for Li_5C is 48.3 K at 210 GPa, but even at 50 GPa, Li_5C has T_c = 14.2 K. It is important to note that superconductivity in lithium−carbon compounds, in general, has small values of T_c. For example, a graphite−Li intercalation compound has T_c = 1.9 K,[26] Li-decorated monolayer graphene has T_c = 5.9 K,[27] and lithium-decorated bilayer graphene has T_c predicted to be 14.7 K.[28] Finally, a vast study for structural lithium carbides at 40 GPa was proposed by Lin et al.[29] and they did not find any structural phase for Li_5C at 40 GPa, which is in accordance with the present study where Li_5C is unstable at this pressure (see Figure S4 in the Supporting Information).

METHODOLOGY

The search and discovery of this material were achieved using the particle swarm optimization method (PSO) with the CALYPSO (Crystal structure AnaLYsis by Particle Swarm Optimization) code[30,31] in the framework of density functional theory (DFT)[32] as implemented in the VASP package.[33] The CALYPSO project uses a stochastic global optimization algorithm with successful applications at predicting new compounds. For Li_5C, we simulated 30 generations of crystal structures at 200 GPa with up to four formula units, totalizing 1500 structures constrained within all space groups. For each generation, 60% of the structures with the smallest enthalpies are used to construct the next generation, while 40% are formed by random structures. The insertion of random structures prevents premature convergence in the PSO algorithm. Each structure is optimized in the VASP package[33] using Perdew−Burke−Ernzerhof (PBE) exchange functionals[34] and projector augmented wave (PAW) pseudopotentials[35] for lithium and carbon with valence configurations $1s^2\ 2s^1\ 2p^0$ and $2s^2\ 2p^2$, respectively. The kinetic energy cutoff for the wave function was 650 eV and the k-spacing tag used was 0.25 $Å^{-1}$ (VASP input tag). It means that the number of k-points in any reciprocal lattice vector is given by $N = \max(1, |\vec{b}_i|/k\text{spacing})$, where $\vec{b}_i \cdot \vec{a}_{ij} = 2\pi\delta_{ij}$ and $\vec{a}_{ij}$ are the real lattice vectors. The k-grid is a Monkhorst−Pack mesh centered at the γ point. After the search, we optimized again the five structures with the lowest enthalpies found (Li_5C in Cm, $C2/m$, $Imm2$, $Immm$, and $P6/mmm$ symmetries), but at this, a finer k-grid (k-spacing = 0.08) was used. For the best structures found, phonon frequencies were analyzed using density functional perturbation theory (DFPT)[36] as implemented in the Quantum ESPRESSO (QE) package.[37,38] Only Li_5C ($P6/mmm$) emerges as a potential stable phase, the other structures were found to be unstable. Therefore, we present Li_5C as a potential global phase at 200 GPa (see structural parameters Table S1 in the Supporting Information). To validate the pseudopotential used at high pressure, the present calculations were compared with the pressure versus volume curve for Li_5C using the LAPW (linearized augmented plane wave) methodology as implemented in the ELK code.[39] The Li_5C structure was relaxed (unit cell and atom positions) by QE in the range from 30 to 250 GPa with steps of 2 GPa. The energy of each relaxed structure was also calculated using the LAPW method, and as a result, the pressure versus volume curve for both methods was compared, as illustrated in Figure S1, showing good agreement between those two methodologies.

For phonon and electron−phonon calculations, we also used PAW pseudopotentials in the GGA approximation at the PBE level, considering three electrons in the valence of lithium ($1s^2\ 2s^1\ 2p^0$) and four electrons in the valence of carbon ([He] $2s^2\ 2p^2$). The kinetic energy cutoff for wave functions was 70 and 350 Ry for charge density cutoff. We used a 28 × 28 × 25 k-grid Monkhorst−Pack mesh centered at the γ point and a 7 × 7 × 5 grid for q-points. Since the calculations for electron−phonon matrix elements require very dense grids, the double grid technique[40] implemented by Wierzbowska et al. in QE was used. This approach has been used successfully in many articles.[41−44] In this approximation, the electron−phonon matrix elements are calculated in a 28 × 28 × 25 k-grid and interpolated in a denser k-grid, 56 × 56 × 50. The coupling parameter λ is calculated by the Eliashberg spectral function $\alpha^2F(\omega)$, which is built from electron−phonon matrix elements. The sigma broadening parameter was 0.01 Ry, which approximates the zero-width limits in the calculation of T_c. A 65 × 65 × 65 k-grid was used for DOS and Fermi surface calculations. To calculate T_c, we used the McMillian formula modified by Allen−Dynes[22] as follow

$$\lambda = \int_0^{\omega_{max}} \frac{2\alpha^2F(\omega)}{\omega} d\omega \tag{1}$$

and T_c is given by

$$T_c = f_1 f_2 \frac{\omega_{log}}{1.2} \exp\left\{-\frac{1.04(1+\lambda)}{\lambda - \mu^*(1+0.62)\lambda}\right\} \tag{2}$$

where ω_{log}, f_1, and f_2 are

$$\omega_{log} = \exp\left\{\frac{2}{\lambda}\int_0^{\omega_{max}} \alpha^2 \ln(\omega)\frac{F(\omega)}{\omega} d\omega\right\} \tag{3}$$

$$f_1 = \sqrt[3]{1 + \left(\frac{\lambda}{2.46(1+3.8\mu^*)}\right)^{3/2}} \tag{4}$$

$$f_2 = \left(1 - \frac{\lambda^2(1+\omega_2/\omega_{log})}{\lambda^2 + 3.312(1+6.3\mu^*)^2}\right) \tag{5}$$

and ω_2 is

$$\omega_2 = \sqrt[2]{\frac{1}{\lambda}\int_0^{\omega_{max}} \frac{2\alpha^2F(\omega)}{\omega}\omega^2 d\omega} \tag{6}$$

The McMillian formula, as modified by Allen−Dynes, is obtained with $f_1 \cdot f_2 = 1$, otherwise, if f_1 and f_2 are calculated as in eqs 4 and 5, we have a "full" Allen−Dynes formula. Figure S2 shows how T_c changes when the Coulomb pseudopotential μ^* varies in the range of 0.10−0.16.

This paper also presents calculations on the hypothetical $(Li_5C)^+$ crystal. Since the periodic system must have a neutral charge to avoid infinite energy repulsion by replication of the unit cell, Quantum ESPRESSO inserts a compensating jellium

https://doi.org/10.1021/acs.jpcc.1c02329
J. Phys. Chem. C 2021, 125, 8899−8906

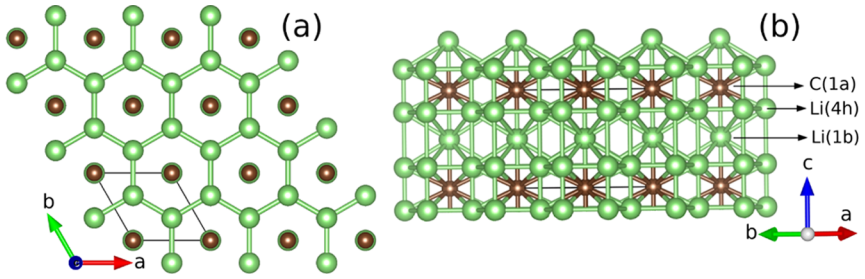

Figure 1. Crystal structure of Li_5C in *P6/mmm* symmetry with two views. Lithium and carbon atoms are colored in green and brown, respectively. (a) View displaying the unit cell. (b) View of the C, Li(4h), and Li(1b) planes.

background to remove energy divergences in case the cell is charged in a periodic system. It is important to note that this homogeneous background charge density is not included explicitly in the calculation of the total charge density in the self-consistency solution. This procedure is equivalent to adding a negative potential to compensate for the energy divergence.

RESULTS AND DISCUSSION

Li_5C is shown in Figure 1 where two perspectives of its structural phase are presented. Li_5C crystallizes in the hexagonal *P6/mmm* space group and according to Wyckoff positions, it has two inequivalent lithium sites and one carbon site. Figure 1a shows lithium atoms at 4h site (1/3, 2/3, 0.782) (green atoms) and carbon at 1a site (0, 0, 0) (brown atoms). Figure 1b displays another perspective and adds Li atoms at 1b site (0, 0, 1/2) (for more structural parameters, see Table S1 in the Supporting Information).

Phonon dispersion curves of Li_5C throughout high symmetrical *q*-points in the first Brillouin zone at various values of pressure (40, 50, 125, 175, 200, 210, and 230 GPa) were calculated and are shown in Figures S3 and S4 in the Supporting Information. The absence of imaginary frequencies in the range of 50−210 GPa indicates stability for Li_5C in *P6/mmm* symmetry. In this material, stability is induced by pressure. However, energy and phonon analysis at 0 K are limited by the lack of statistical fluctuation. Therefore, to overcome this difficulty, we also employed Car and Parrinello molecular dynamics[45] with a Nosé−Hoover thermostat,[46] thus simulating 384 atoms in the canonical ensemble (a supercell with 4 × 4 × 4 dimensions) to further ascertain the stability of the structures. The result is illustrated in Figure 2, in which root-mean-square deviation (RMSD) calculated by the atomic displacements shows large stability. For instance, time-averaged RMSD values, compared to perfect structures at 0 K and 200 GPa, achieve 0.08, 0.09, and 0.12 Å at temperatures of 50, 150, and 300 K, respectively; therefore, Li_5C in the *P6/mmm* phase maintained its stability even at 300 K simulation. Molecular dynamics calculations were performed in different situations: (i) The simulation starts at 200 GPa and after thermalization at 300 K, the pressure reaches an average of 203.5 GPa (see Figure S4b and Video in the Supporting Information). The same procedure is repeated for thermalization at 50 and 150 K. (ii) Simulations start at 50 GPa and 300 K and achieve a pressure of around 51.2 GPa after thermalization (Figure S5 in the Supporting Information). In these calculations, the size of the supercell was taken to be large enough to guarantee statistical fluctuations and consistent results when compared with the present DFT calculations. In summary, even assuming very small tolerances, the crystal kept

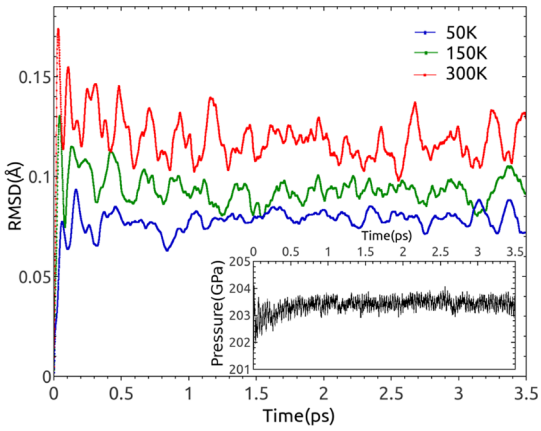

Figure 2. How root-mean-square deviation (RMSD) changes in time for 50 (blue line), 150 (green line), and 300 K (red line). The inset shows how pressure is stabilized in time when the simulation started at 200 GPa.

the same structural phase in various thermodynamic conditions.

Although the convex hull (composition phase diagram) is not present in this study, which could indicate a possible phase decomposition, large molecular dynamics simulations presented are robust to indicate that Li_5C is not decomposed in other phases because high energy barriers may exist in the pathway for Li_5C decomposition and explain such strong stability presented in this compound. The convex hull is, in principle, a very important condition to indicate a stable phase. However, the convex hull methodology is unable to display the curve of the energy barrier that exists in the pathway between crystalline phases, as well as it is unable to indicate dynamical stability including temperature effects. Diverse experimental techniques show that even crystalline phases that have enthalpies above the convex hull are possible to be synthesized in the laboratory. For instance, methods like laser irradiation combined with pressure imposed by a diamond anvil cell (DAC) have been used to synthesize various metastable phases.[47] Diverse techniques are used to produce carbon allotropes like diamond, graphene, and other structures. Exotic silicon phases have also been frequently synthesized in laboratories.[48] This idea is also valid for some metallic compounds that do not sit on the convex hull but also can be synthesized.[49] All these findings and recent advances in chemistry and physics of materials reveal that although the convex hull is a theoretically important condition to find stable phases in nature, it is not a necessary condition to obtain manipulated phases in the laboratory. In addition, the exploration of metastable phases also represents a route to

https://doi.org/10.1021/acs.jpcc.1c02329
J. Phys. Chem. C 2021, 125, 8899−8906

design materials with improved superconducting properties.[50] The stability presented here for Li_5C opens research possibilities for further investigation in Li−C systems at ultrahigh pressures.

Li_5C is a 2D electride with interstitial anionic electrons forming a 2D confined structure in the (0001) plane, containing Li atoms at 1b site (layers formed by Li at 1b site). In a simplified way of understanding, the unit cell has five lithium atoms and one carbon atom. Carbon atoms only absorb four electrons from four lithium atoms at 4h sites. These lithium atoms at 4h sites are completely ionized in the same way as classical ionic compounds, forming a hexagonal cationic layer that is responsible for inducing confined hexagonal interstitial anionic electrons. These confined electrons are located in the interstitial sites of the adjacent layer formed by Li at 1b sites. The electride can be understood by the formula $[Li_5C]^+(e^-)$. This effect only occurs at high pressures, starting at 50 GPa.

Electron localization function (ELF) is a suitable method for distinguishing localized electrons, electron gas, or delocalized wave functions (itinerant electrons).[52] Therefore, it was used to illustrate and explain how the electride state can be understood. In this material, near carbon atoms, the ELF value is next to 1, indicating high localized electrons. On the other hand, around lithium atoms, ELF is below 0.5 and tends to 0 near these alkali atoms, except for cores due to pseudopotentials. However, a new situation appears when we analyze the ELF color map in the interstitial sites of the crystal. Figure 3a presents a slice in the (0001) plane formed by Li atoms at 1b sites at 50 GPa. Region A indicated in Figure 3a shows localized ELF values around 0.77, and in region B, ELF is approximately 0.63. It is important to point out that these localized electrons (electron pockets) only appear in the interstitial site in the region of slices, as shown in Figure 3a, that is formed by Li atoms at 1b sites, as shown in Figure 1 (consider a slice with a small thickness). The rest of the crystal seems to be a typical ionic material in ELF analysis. To confirm the electride state, we created a hypothetical crystal $(Li_5C)^+$ and analyzed ELF again. As a result, all regions of the crystal in the ELF analyses remained the same as in Li_5C, except for the slice shown in Figure 3b where the ELF values are clearly reduced mainly in the interstitial site (see Figure S6 in the Supporting Information).

Similar analyses are repeated in Figure 3c,d using the charge density difference map (CDD) for Li_5C and $(Li_5C)^+$, respectively. Although CDD presents very similar results, in agreement with ELF, it has a completely different meaning: while ELF shows localized or delocalized electrons, CDD shows the charge density difference removing the contribution of the isolated atoms. Therefore, combining ELF and CDD calculations, we observe that the excess of electrons reside in the interstitial layer formed by Li at 1b site, this being a very specific region of space. This situation becomes more explicit with the perspective image displayed in Figure 3e,f, for ELF = 0.65 and CDD = 0.0001 e/Å^3 isovalues, an entirely connected hexagonal anionic electron geometry made by electrons in the interstitial sites of the crystal, confined in a plane with an estimated thickness of 1.8 Å. This is the result of the hexagonal cationic layer formed by lithium at 4h site that produces quantum confinement at an adjacent Li layer; it induces electron pockets in the interstitial sites of the crystal. We also observe that when pressure increases, the hexagonal anionic electrons evolve to the electron gas. It suggests a relationship

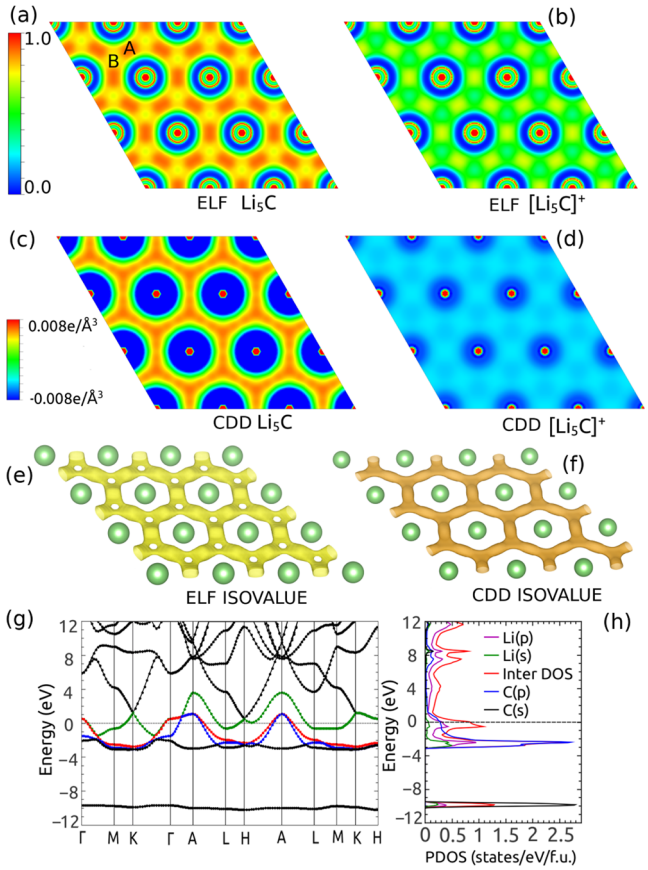

Figure 3. (a) ELF map for Li_5C at 50 GPa in the (0001) plane generated by Li at 1b site. (b) The same as presented in (a), but the analysis is done for $(Li_5C)^+$. (c) Charge density difference map at 50 GPa in the (0001) Li plane generated by Li at 1b site. (d) The same slice as shown in (c), but the analysis is done for $(Li_5C)^+$. (e) Hexagonal ELF in perspective at a 0.65 isovalue emerged in the (0001) plane, which contained Li at 1b site. (f) Hexagonal CDD at a 0.0001 e/Å^3 isovalue in the same plane displayed in (e). (g) Band structure for Li_5C. Three bands are colored in blue, red, and green representing the first, second, and third bands crossing the Fermi level, respectively. (h) PDOS and interstitial DOS (IDOS) calculated using a full-potential LAPW by the ELK code using a muffin-tin radius of 0.9 Å. Visualization was made in VESTA.[51]

between high electron mobility and high T_c values at 210 GPa. Others ELF and CDD plots are shown in Figures S7−S9 in the Supporting Information considering different values of pressure and different isovalues.

We also discuss the electronic structure aspects related to the appearance of the electride state in Li_5C, which are presented in Figure 3a−f. Figure 3g,h shows the band structure and respective projected density of states (PDOS) at 200 GPa. The Li_5C band structure has valence and conduction bands crossing the Fermi level as expected for a metal (no band gap), and highly dispersive half fill bands near the Fermi level are observed for diverse high symmetrical *k*-lines, mainly in Γ → A and Γ → K lines. In Figure 3h, the higher contribution for total DOS at the Fermi level comes from the interstitial electron contribution (IDOS). In Figure 4, PDOS calculated for Li atoms at 1b site shows that the p-orbital contribution is greater than the s-orbital contribution, the same occurs for lithium at site 4h near the Fermi level. The s-orbital signal is reduced, while the p-orbital signal increases. Comparatively, the effects on the electronic charges in the Li 1b plane are such that the

https://doi.org/10.1021/acs.jpcc.1c02329
J. Phys. Chem. C 2021, 125, 8899−8906

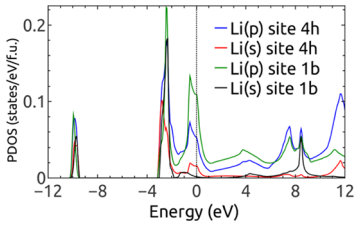

Figure 4. PDOS for lithium at 1b site and lithium at 4h site.

lithium at 1b site has a stronger transition from s to the p character than lithium at 4h site. Therefore, an important (signal) contribution for PDOS near the Fermi level comes from Li at 1b site, which is in the same plane of the hexagonal anionic electrons. The electride state is responsible for this transition from s to p at the (0001) plane.

To evaluate how the density of states is connected with electron pockets, the integrated local density of states (ILDOS) was calculated from −1 eV to the Fermi level and is shown in Figure 5a. The maximum value of ILDOS is found in the same region of the electron pockets with the same topology previously shown in ELF and CDD calculations. Furthermore, outside 1b lithium planes, ILDOS is very close to 0, thus indicating that the high amount of available states is restricted to the region in the planes formed by lithium atoms at 1b site in accordance with Figure 5b. Therefore, high conductivity or conventional superconductivity cannot arise from another part of this crystal, except from the connected electron pockets. The ILDOS for $(Li_5C)^+$ was also evaluated and is shown in Figure 5c,d. It clearly indicates a strong reduction of the ILDOS in the region of electron pockets, corroborating that the high amount of states comes from electride anionic states.

It was shown in recent works that electrides under pressure may show superconductivity; therefore, we investigated Li_5C studying the superconducting transition temperature T_c. To achieve these results, Eliashberg's formulation,[20] as implemented by McMillan[21] and Allen−Dynes,[22] was employed. Figure 6a shows the Eliashberg spectral function at 210 GPa. The integrated electron−phonon coupling parameter λ reaches values up to 1.26 at 210 GPa. It shows a peak at around 5 THz and the main contribution for λ (more than 50%) comes from 3 to 10 THz phonon frequencies. This behavior is observed for diverse values of pressure. For instance, at 50 GPa, λ = 0.66, but it reaches λ = 0.35 up to 10 THz. Figure 3b shows the superconducting transition temperature T_c as a function of pressure calculated by McMillan and Allen−Dynes formulae.[21,22] The spectral function is also displayed for many different values of pressure in Figure S10 in the Supporting Information. In Figure 6b, we can see that T_c increases with pressure, indicating that pressure can be used as a macroscopic parameter to modulate T_c. The maximum value achieved for T_c is 48.3 K at 210 GPa (μ^* = 0.1). The dependence of T_c when μ^* changes is shown in the Supporting Information. Phonon frequencies for Li_5C at 210 GPa are shown in many high symmetric directions in Figure 6c. The analysis of partial electron−phonon coupling parameter corroborates that the vibrational modes that have a stronger contribution for the EP parameter are associated with low-frequency modes.

Finally, the Fermi surface (FS) topology is connected to the band structure and also related to superconductivity. In Figure 6d−f, we show the FS for three bands crossing the Fermi level. The bandwidths of the bands crossing the Fermi level that are related to the Fermi surface are 4.14, 3.82, and 5.01 eV, which are, respectively, represented in Figure 6d−f. Figure 6d shows an FS shaped in two cylindrical lobes along the Γ−A line; in this FS, we can see a nesting surface with a nesting vector parallel to the Γ → A line. A nesting surface is also shown in Figure 6e, where the FS also resembles a cylindrical shape with a reduced radius in the central region. Figure 6f shows an FS with a cylindrical hole at the center connecting two parts of an approximately flat FS band. This FS band shown in Figure 6f also has a cylindrical hole around the H−K line (Figure S11 shows the extended FS in the Supporting Information). These FS bands lead to possible electron pairing with intraband interactions (electron pairing interaction within the same band); this mechanism can boost the T_c value. Figure 6g shows beyond the single band scenario and displays merged bands. A couple of interband FSs are clearly observed by the formation of two very close concentric cylindrical Fermi surfaces along the Γ−A line. Many articles have shown that the FS topology can be strongly related to a multiband mechanism, enhancing electron−phonon coupling.[54−57] In the multiband mechanism, electron pairing does not occur only due to the intraband but also due to the interband interaction. These two very close concentric cylindrical Fermi surfaces (without an overlap) suggest a correlation with electron−phonon coupling and strong intraband and interband pairing interactions, leading to

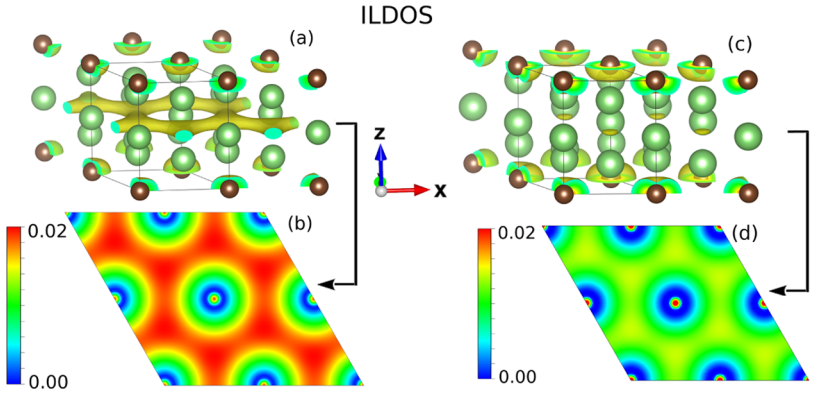

Figure 5. (a) Three-dimensional ILDOS plot at a 0.018 isovalue for Li_5C at 200 GPa. (b) Two-dimensional color map for ILDOS; the slice for the (0001) plane at 1b lithium sites. (c) Three-dimensional ILDOS plot at a 0.014 isovalue for $(Li_5C)^+$ at 200 GPa. (d) Two-dimensional color map for ILDOS; the slice for the (0001) plane at 1b lithium sites. The results are in atomic Rydberg units.

https://doi.org/10.1021/acs.jpcc.1c02329
J. Phys. Chem. C 2021, 125, 8899−8906

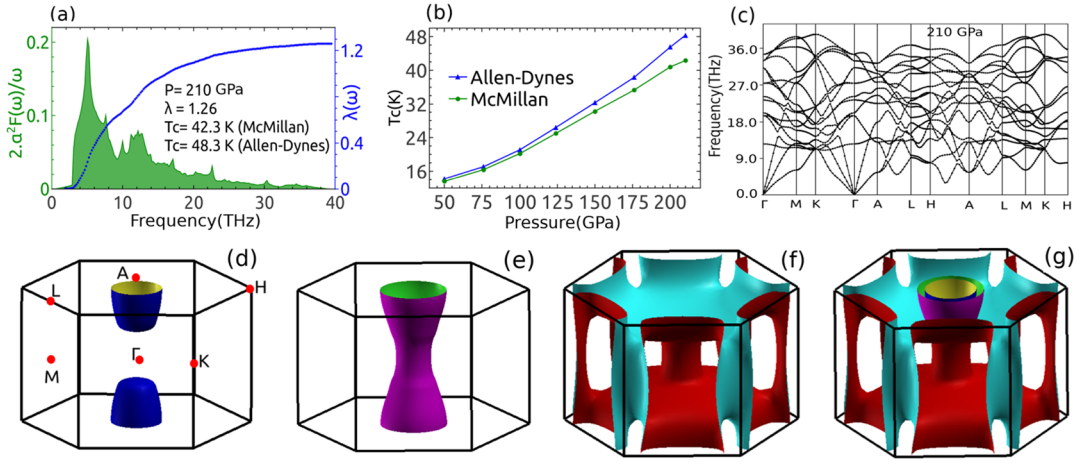

Figure 6. (a) Eliashberg spectral function in the green area ($2{\cdot}a^2F(\omega)/\omega$), while the blue line shows how λ increases by the integration of the spectral function at 210 GPa. (b) T_c versus pressure curve; the blue line is the Allen−Dynes formula and the green line is the McMillan formula modified by Allen−Dynes; the used Coulomb pseudopotential parameter is $\mu^* = 0.1$. (c) Phonon frequencies for Li_5C at 210 GPa are displayed in many high-symmetry directions, as suggested by Setyawan.[53] (d−f) Fermi surface (FS) for three conduction bands crossing the Fermi level. (g) FS merged for all bands shown in (d), (e), and (f).

Li_5C having a high predicted T_c value, well above the McMillan limit. Although the band structure and the FS indicate a metallic behavior in all directions of this crystal, these concentric cylinders formed with warped lines along the Γ → A line indicate strong metallicity in a 2D plane,[58] which corresponds to the same plane of the hexagonal anionic density. Therefore, the FS is well defined and connected to dispersive bands at the Fermi level and a high T_c value. Similar multiband mechanisms can be also found in magnesium diboride (MgB_2 with T_c = 39 K), which also has a couple of cylindrical FSs around the Γ−A line.[59,60]

CONCLUSIONS

In summary, we found a potential new electride superconductor at megabar pressure. Li_5C has remarkable electronic properties and high T_c superconductivity. This predicted material has a particular 2D confined hexagonal ionic density topology similar to a quantum confinement electron problem. This characteristic allows Li_5C to have high conductivity not observed in typical ionic materials, leading to an elevated T_c value never reported before for this kind of compound.

ASSOCIATED CONTENT

Supporting Information

The Supporting Information is available free of charge at https://pubs.acs.org/doi/10.1021/acs.jpcc.1c02329.

Figures related to methodology; details of dynamics stability, electronic structure, and electron−phonon coupling (PDF)

Video presents a molecular dynamics simulation at 203.5 GPa at 300 K (perspective 1) (MPG)

Video presents a molecular dynamics simulation at 203.5 GPa at 300 K (perspective 2) (MPG)

AUTHOR INFORMATION

Corresponding Author

Edison Z. da Silva − *Institute of Physics "Gleb Wataghin", UNICAMP, 13083-859 Campinas, SP, Brazil;* orcid.org/0000-0002-2195-0051; Email: zacarias@ifi.unicamp.br

Authors

Zenner S. Pereira − *Departamento de Ciência e Tecnologia, Universidade Federal Rural do Semi-Árido (UFERSA), 59780-000 Campus Caraúbas, RN, Brazil;* orcid.org/0000-0002-9253-6341

Giovani M. Faccin − *Faculdade de Ciências Exatas e Tecnológicas, Universidade Federal da Grande Dourados (UFGD)—Unidade II, 79804-970 Dourados, MS, Brazil; Institute of Physics "Gleb Wataghin", UNICAMP, 13083-859 Campinas, SP, Brazil;* orcid.org/0000-0003-1864-2434

Complete contact information is available at: https://pubs.acs.org/10.1021/acs.jpcc.1c02329

Notes

The authors declare no competing financial interest.

ACKNOWLEDGMENTS

The simulations were performed at the CCJDR-Unicamp computers, CENAPAD-SP and SDumont—Sistema de Computação Santos Dumont(LNCC). The authors acknowledge support from FAPESP (2013/07296-2, 2016/23891-6, and 2017/26105-4) and CNPq and UFERSA-CARAÚBAS (23091.004584/2021-94). Cover Art by Desayuno.

REFERENCES

(1) Dye, J. L. Electrides: Early Examples of Quantum Confinement. *Acc. Chem. Res.* **2009**, *42*, 1564−1572.

(2) Zhang, Y.; Xiao, Z.; Kamiya, T.; Hosono, H. Electron Confinement in Channel Spaces for One-Dimensional Electride. *J. Phys. Chem. Lett.* **2015**, *6*, 4966−4971.

(3) Matsuishi, S.; Toda, Y.; Miyakawa, M.; Hayashi, K.; Kamiya, T.; Hirano, M.; Tanaka, I.; Hosono, H. High-Density Electron Anions in a Nanoporous Single Crystal: $[Ca_{24}Al_{28}O_{64}]4+(4e-)$. *Science* **2003**, *301*, 626−629.

(4) Liu, C.; Nikolaev, S. A.; Ren, W.; Burton, L. A. Electrides: a review. *J. Mater. Chem. C* **2020**, *8*, 10551−10567.

(5) Zhang, X.; Yang, G. Recent Advances and Applications of Inorganic Electrides. *J. Phys. Chem. Lett.* **2020**, *11*, 3841−3852.

(6) Toda, Y.; Kim, S. W.; Hayashi, K.; Hirano, M.; Kamiya, T.; Hosono, H.; Haraguchi, T.; Yasuda, H. Intense thermal field electron

emission from room-temperature stable electride. *Appl. Phys. Lett.* **2005**, *87*, No. 254103.
(7) Hu, J.; Xu, B.; Yang, S. A.; Guan, S.; Ouyang, C.; Yao, Y. 2D Electrides as Promising Anode Materials for Na-Ion Batteries from First-Principles Study. *ACS Appl. Mater. Interfaces* **2015**, *7*, 24016−24022.
(8) Hou, J.; Tu, K.; Chen, Z. Two-Dimensional Y2C Electride: A Promising Anode Material for Na-Ion Batteries. *J. Phys. Chem. C* **2016**, *120*, 18473−18478.
(9) Shimizu, K.; Ishikawa, H.; Takao, D.; Yagi, T.; Amaya, K. Superconductivity in compressed lithium at 20 K. *Nature* **2002**, *419*, 597−599.
(10) Xie, Y.; Oganov, A. R.; Ma, Y. Novel High Pressure Structures and Superconductivity of $CaLi_2$. *Phys. Rev. Lett.* **2010**, *104*, No. 177005.
(11) Li, X.; Hermann, A.; Peng, F.; Lv, J.; Wang, Y.; Wang, H.; Ma, Y. Stable Lithium Argon compounds under high pressure. *Sci. Rep.* **2015**, *5*, No. 16675.
(12) Kokail, C.; Heil, C.; Boeri, L. Search for high-T_c conventional superconductivity at megabar pressures in the lithium-sulfur system. *Phys. Rev. B* **2016**, *94*, No. 060502.
(13) Zhao, Z.; Zhang, S.; Yu, T.; Xu, H.; Bergara, A.; Yang, G. Predicted Pressure-Induced Superconducting Transition in Electride Li_6P. *Phys. Rev. Lett.* **2019**, *122*, No. 097002.
(14) Toda, Y.; Hirayama, H.; Kuganathan, N.; Torrisi, A.; Sushko, P. V.; Hosono, H. Activation and splitting of carbon dioxide on the surface of an inorganic electride material. *Nat. Commun.* **2013**, *4*, No. 2378.
(15) Hosono, H.; Kim, J.; Toda, Y.; Kamiya, T.; Watanabe, S. *Proc. Natl. Acad. Sci. U.S.A.* **2017**, *114*, 233−238.
(16) Lee, K.; Kim, S. W.; Toda, Y.; Matsuishi, S.; Hosono, H. Dicalcium nitride as a two-dimensional electride with an anionic electron layer. *Nature* **2013**, *494*, 336−340.
(17) Zhao, S.; Li, Z.; Yang, J. Obtaining Two-Dimensional Electron Gas in Free Space without Resorting to Electron Doping: An Electride Based Design. *J. Am. Chem. Soc.* **2014**, *136*, 13313−13318.
(18) Bardeen, J.; Cooper, L.; Schrieffer, J. Theory of superconductivity. *Phys. Rev.* **1957**, *108*, 1175−1204.
(19) Gorkov, L. On The Energy Spectrum Of Superconductors. *Sov. Phys. JETP-USSR* **1958**, *7*, 505−508.
(20) Eliashberg, G. Interactions Between Electrons and Lattice Vibrations on a Superconductor. *Sov. Phys. JETP-USSR* **1960**, *11*, 697−702.
(21) McMillan, W. L. Transition Temperature of Strong-Coupled Superconductors. *Phys. Rev.* **1968**, *167*, 331−344.
(22) Allen, P. B.; Dynes, R. C. Transition temperature of strong-coupled superconductors reanalyzed. *Phys. Rev. B* **1975**, *12*, 905−922.
(23) Miyakawa, M.; Kim, S. W.; Hirano, M.; Kohama, Y.; Kawaji, H.; Atake, T.; Ikegami, H.; Kono, K.; Hosono, H. Superconductivity in an Inorganic Electride $12CaO{\cdot}7Al_2O_3$:e-. *J. Am. Chem. Soc.* **2007**, *129*, 7270−7271.
(24) Sa, B.; Xiong, R.; Wen, C.; Li, Y.-L.; Lin, P.; Lin, Q.; Anpo, M.; Sun, Z. Electronic Anisotropy and Superconductivity in One-Dimensional Electride Ca_3Si. *J. Phys. Chem. C* **2020**, *124*, 7683−7690.
(25) Shao, S.; Zhu, W.; Lv, J.; Wang, Y.; Chen, Y.; Ma, Y. The exotically stoichiometric compounds in Al−S system under high pressure. *npj Comput. Mater.* **2020**, *6*, No. 11.
(26) Belash, I.; Bronnikov, A.; Zharikov, O.; Pal'nichenko, A. Superconductivity of graphite intercalation compound with lithium C_2Li. *Solid State Commun.* **1989**, *69*, 921−923.
(27) Ludbrook, B. M.; Levy, G.; Nigge, P.; Zonno, M.; Schneider, M.; Dvorak, D. J.; Veenstra, C. N.; Zhdanovich, S.; Wong, D.; Dosanjh, P.; et al. *Proc. Natl. Acad. Sci. U.S.A.* **2015**, *112*, 11795−11799.
(28) Szczęśniak, D. *EPL* **2015**, *111*, No. 18003.
(29) Lin, Y.; Strobel, T. A.; Cohen, R. E. Structural diversity in lithium carbides. *Phys. Rev. B* **2015**, *92*, No. 214106.
(30) Wang, Y.; Lv, J.; Zhu, L.; Ma, Y. Crystal structure prediction via particle-swarm optimization. *Phys. Rev. B* **2010**, *82*, No. 094116.
(31) Wang, Y.; Lv, J.; Zhu, L.; Ma, Y. CALYPSO: A method for crystal structure prediction. *Comput. Phys. Commun.* **2012**, *183*, 2063−2070.
(32) Kohn, W.; Sham, L. J. Self-Consistent Equations Including Exchange and Correlation Effects. *Phys. Rev.* **1965**, *140*, A1133−A1138.
(33) Kresse, G.; Furthmüller, J. Efficient iterative schemes for ab initio total-energy calculations using a plane-wave basis set. *Phys. Rev. B* **1996**, *54*, 11169−11186.
(34) Perdew, J. P.; Burke, K.; Ernzerhof, M. Generalized Gradient Approximation Made Simple. *Phys. Rev. Lett.* **1996**, *77*, 3865−3868.
(35) Blöchl, P. E. Projector augmented-wave method. *Phys. Rev. B* **1994**, *50*, 17953−17979.
(36) Baroni, S.; de Gironcoli, S.; Dal Corso, A.; Giannozzi, P. Phonons and related crystal properties from density-functional perturbation theory. *Rev. Mod. Phys.* **2001**, *73*, 515−562.
(37) Giannozzi, P.; Baroni, S.; Bonini, N.; Calandra, M.; Car, R.; Cavazzoni, C.; Ceresoli, D.; Chiarotti, G. L.; Cococcioni, M.; Dabo, I.; et al. QUANTUM ESPRESSO: a modular and open-source software project for quantum simulations of materials. *J. Phys.: Condens. Matter* **2009**, *21*, No. 395502.
(38) Giannozzi, P.; Andreussi, O.; Brumme, T.; Bunau, O.; Nardelli, M. B.; Calandra, M.; Car, R.; Cavazzoni, C.; Ceresoli, D.; Cococcioni, M.; et al. Advanced capabilities for materials modelling with Quantum ESPRESSO. *J. Phys.: Condens. Matter* **2017**, *29*, No. 465901.
(39) Müller, T.; Sharma, S.; Gross, E. K. U.; Dewhurst, J. K. Extending Solid-State Calculations to Ultra-Long-Range Length Scales. *Phys. Rev. Lett.* **2020**, *125*, No. 256402.
(40) Wierzbowska, M.; de Gironcoli, S.; Giannozzi, P. Origins of Low- and High-Pressure Discontinuities of T_c in Niobium, arXiv:cond-mat/0504077. arXiv.org e-Print archive. https://arxiv.org/abs/cond-mat/0504077 (submitted April 04, 2005).
(41) Salke, N. P.; Davari Esfahani, M. M.; Zhang, Y.; Kruglov, I. A.; Zhou, J.; Wang, Y.; Greenberg, E.; Prakapenka, V. B.; Liu, J.; Oganov, A. R.; et al. Synthesis of clathrate cerium superhydride CeH_9 at 80−100 GPa with atomic hydrogen sublattice. *Nat. Commun.* **2019**, *10*, No. 4453.
(42) Yu, H.; Lin, X.; Li, K.; Chen, Y. Unveiling a Novel, Cation-Rich Compound in a High-Pressure Pb−Te Binary System. *ACS Cent. Sci.* **2019**, *5*, 683−687.
(43) Yu, H.; Chen, Y. Unexpected High-Pressure Phase of GeTe with an Origin of Low Ionicity and Electron Delocalization. *J. Phys. Chem. C* **2018**, *122*, 15673−15677.
(44) Hayami, W.; Tanaka, T. Superconductivity of alkali-metal intercalated BC2. *AIP Adv.* **2020**, *10*, No. 065213.
(45) Car, R.; Parrinello, M. Unified Approach for Molecular Dynamics and Density-Functional Theory. *Phys. Rev. Lett.* **1985**, *55*, 2471−2474.
(46) Hoover, W. G. Canonical dynamics: Equilibrium phase-space distributions. *Phys. Rev. A* **1985**, *31*, 1695−1697.
(47) Solozhenko, V. L.; Kurakevych, O. O.; Andrault, D.; Le Godec, Y.; Mezouar, M. Ultimate Metastable Solubility of Boron in Diamond: Synthesis of Superhard Diamondlike BC_5. *Phys. Rev. Lett.* **2009**, *102*, No. 015506.
(48) Smillie, L. A.; Niihori, M.; Rapp, L.; Haberl, B.; Williams, J. S.; Bradby, J. E.; Pickard, C. J.; Rode, A. V. Exotic silicon phases synthesized through ultrashort laser-induced microexplosion: Characterization with Raman microspectroscopy. *Phys. Rev. Mater.* **2020**, *4*, No. 093803.
(49) Delmonte, D.; Mezzadri, F.; Spaggiari, G.; Rampino, S.; Pattini, F.; Bersani, D.; Gilioli, E. Metastable (CuAu-type) $CuInS_2$ Phase: High-Pressure Synthesis and Structure Determination. *Inorg. Chem.* **2020**, *59*, 11670−11675.
(50) Flores-Livas, J. A.; Sanna, A.; Drozdov, A. P.; Boeri, L.; Profeta, G.; Eremets, M.; Goedecker, S. Interplay between structure and superconductivity: Metastable phases of phosphorus under pressure. *Phys. Rev. Mater.* **2017**, *1*, No. 024802.

https://doi.org/10.1021/acs.jpcc.1c02329
J. Phys. Chem. C 2021, 125, 8899−8906

(51) Momma, K.; Izumi, F. *VESTA3* for three-dimensional visualization of crystal, volumetric and morphology data. *J. Appl. Crystallogr.* **2011**, *44*, 1272−1276.
(52) Becke, A. D.; Edgecombe, K. E. A simple measure of electron localization in atomic and molecular systems. *J. Chem. Phys.* **1990**, *92*, 5397−5403.
(53) Setyawan, W.; Curtarolo, S. High-throughput electronic band structure calculations: Challenges and tools. *Comput. Mater. Sci.* **2010**, *49*, 299−312.
(54) Whangbo, M.-H.; Deng, S.; Köhler, J.; Simon, A. Interband Electron Pairing for Superconductivity from the Breakdown of the Born−Oppenheimer Approximation. *ChemPhysChem* **2018**, *19*, 3191−3195.
(55) Dolgov, O. V.; Mazin, I. I.; Parker, D.; Golubov, A. A. Interband superconductivity: Contrasts between Bardeen−Cooper−Schrieffer and Eliashberg theories. *Phys. Rev. B* **2009**, *79*, No. 060502.
(56) Li, Y.; Liu, M.; Fu, Z.; Chen, X.; Yang, F.; Yang, Y.-f. Gap Symmetry of the Heavy Fermion Superconductor $CeCu_2Si_2$ at Ambient Pressure. *Phys. Rev. Lett.* **2018**, *120*, No. 217001.
(57) Machida, M.; Nakamura, H. Two-dimensionality of electronic structure and strong Fermi surface nesting in highly anisotropic iron-based superconductors. *Phys. C* **2010**, *470*, 1002−1006.
(58) Canadell, E. Dimensionality and Fermi Surface of Low-Dimensional Metals. *Chem. Mater.* **1998**, *10*, 2770−2786.
(59) Geerk, J.; Schneider, R.; Linker, G.; Zaitsev, A. G.; Heid, R.; Bohnen, K.-P.; Löhneysen, H. V. Observation of Interband Pairing Interaction in a Two-Band Superconductor: MgB_2. *Phys. Rev. Lett.* **2005**, *94*, No. 227005.
(60) Mazin, I.; Antropov, V. Electronic structure, electron−phonon coupling, and multiband effects in MgB_2. *Phys. C* **2003**, *385*, 49−65.

https://doi.org/10.1021/acs.jpcc.1c02329
J. Phys. Chem. C 2021, 125, 8899−8906